The MJO Transition from Shallow to Deep Convection in *CloudSat*/CALIPSO Data and GISS GCM Simulations

ANTHONY D. DEL GENIO

NASA Goddard Institute for Space Studies, New York, New York

YONGHUA CHEN

Department of Applied Physics and Applied Mathematics, Columbia University, New York, New York

DAEHYUN KIM

Lamont-Doherty Earth Observatory, Columbia University, Palisades, New York

MAO-SUNG YAO

Sigma Space Partners, Institute for Space Studies, New York, New York

(Manuscript received 12 July 2011, in final form 26 September 2011)

ABSTRACT

The relationship between convective penetration depth and tropospheric humidity is central to recent theories of the Madden–Julian oscillation (MJO). It has been suggested that general circulation models (GCMs) poorly simulate the MJO because they fail to gradually moisten the troposphere by shallow convection and simulate a slow transition to deep convection. *CloudSat* and Cloud–Aerosol Lidar and Infrared Pathfinder Satellite Observations (CALIPSO) data are analyzed to document the variability of convection depth and its relation to water vapor during the MJO transition from shallow to deep convection and to constrain GCM cumulus parameterizations. Composites of cloud occurrence for 10 MJO events show the following anticipated MJO cloud structure: shallow and congestus clouds in advance of the peak, deep clouds near the peak, and upper-level anvils after the peak. Cirrus clouds are also frequent in advance of the peak. The Advanced Microwave Scanning Radiometer for Earth Observing System (EOS) (AMSR-E) column water vapor (CWV) increases by ~5 mm during the shallow–deep transition phase, consistent with the idea of moisture preconditioning. Echo-top height of clouds rooted in the boundary layer increases sharply with CWV, with large variability in depth when CWV is between ~46 and 68 mm. International Satellite Cloud Climatology Project cloud classifications reproduce these climatological relationships but correctly identify congestus-dominated scenes only about half the time. A version of the Goddard Institute for Space Studies Model E2 (GISS-E2) GCM with strengthened entrainment and rain evaporation that produces MJO-like variability also reproduces the shallow–deep convection transition, including the large variability of cloud-top height at intermediate CWV values. The variability is due to small grid-scale relative humidity and lapse rate anomalies for similar values of CWV.

1. Introduction

The Madden–Julian oscillation (MJO; Madden and Julian 1971), a slowly eastward-propagating envelope that modulates tropical precipitation in boreal winter on time scales of 20–90 days from the Indian Ocean to the West Pacific, is the primary source of subseasonal rainfall variability in the tropics. The MJO has captured the attention of tropical meteorologists for several decades. It does not lie along dispersion curves for linear equatorial waves, as do other observed convectively coupled equatorial waves (Wheeler and Kiladis 1999), and thus a plethora of theories have been advanced to explain its initiation, propagation direction and speed, vertical structure, and decay (e.g., see the review by Zhang 2005). Furthermore, the MJO has generally been poorly, if at all, simulated by several generations of operational general

Corresponding author address: Anthony D. Del Genio, NASA Goddard Institute for Space Studies, 2880 Broadway, New York, NY 10025.
E-mail: anthony.d.delgenio@nasa.gov

DOI: 10.1175/JCLI-D-11-00384.1

circulation models (GCMs) (Slingo et al. 1996; Sperber et al. 2005; Lin et al. 2006; Kim et al. 2009; Mapes and Bacmeister 2012).

One class of ideas about the MJO invokes the so-called ''recharge–discharge'' mechanism by which convection interacts with tropospheric humidity to regulate precipitation on intraseasonal time scales (Bladé and Hartmann 1993; Hu and Randall 1994; Kemball-Cook and Weare 2001; Stephens et al. 2004; Benedict and Randall 2007). In this framework, shallow convection dominates under suppressed conditions because dry air entrained into the updraft evaporates cloud water, reducing the buoyancy of the updraft and limiting its ascent. However, the saturated air detrained by the cumulus moistens the troposphere near the detrainment level, supplemented by evaporation of any light rain. This produces a more humid and favorable environment for later convective events, which penetrate somewhat higher and moisten higher altitudes until eventually the column has been moistened sufficiently that deep convection can be triggered. This transition to the disturbed phase of the MJO brings heavy precipitation that eventually discharges the tropospheric moisture, returning the atmosphere to the dry suppressed state. Simple dynamical models that utilize an assumed interaction between tropospheric moisture and precipitation or the diabatic heating profile have had success producing MJO-like behavior (e.g., Khouider and Majda 2006; Kuang 2008; Raymond et al. 2009).

GCMs have traditionally focused primarily on deep convection and assumed weak entrainment to allow convection to penetrate to the tropopause. Derbyshire et al. (2004) demonstrated that these models do not produce the sensitivity of convection depth to tropospheric humidity that occurs in cloud-resolving models. The fact that GCMs poorly simulate the MJO may thus not be a surprise in light of this result. Indeed, several studies have shown that behavior consistent with the MJO is typical of models that have a tighter link between convection and humidity because of strong convective entrainment or rain evaporation (Bechtold et al. 2008; Kim et al. 2009, 2011a; Hannah and Maloney 2011) or that embed a cloud-resolving model within GCM gridboxes (Khairoutdinov et al. 2008; Thayer-Calder and Randall 2009; Zhu et al. 2009).

Observational evidence for the link between increasing tropospheric humidity and increasing convection depth during the transition from the suppressed to the disturbed phase of the MJO has accumulated in recent years. Kikuchi and Takayabu (2004), Kiladis et al. (2005), Mapes et al. (2006), Morita et al. (2006), Benedict and Randall (2007), Lau and Wu (2010), and Tian et al. (2010) show evidence of an upward–westward tilt in the structure of temperature, humidity, precipitation radar echo height and diabatic heating anomalies as MJO phase progresses. Other studies have documented the variation of precipitation and the humidity profile with column water vapor in the tropics (Bretherton et al. 2004; Holloway and Neelin 2009) but not specific to the MJO. Jensen and Del Genio (2006) and Holloway and Neelin (2009) have shown relationships between humidity and convection depth, again not specific to the MJO and at a location (Nauru Island) on the eastern fringe of the region affected by the MJO. International Satellite Cloud Climatology Project (ISCCP) cloud classifications aggregated by MJO phase (Chen and Del Genio 2009; Tromeur and Rossow 2010) exhibit greater shallow and congestus–disorganized convection occurrence during the suppressed and developing phases relative to the disturbed phase, as do Geostationary Meteorological Satellite infrared brightness temperatures (Kikuchi and Takayabu 2004). However, the passive remote sensing data used to define these states have limited information on actual cloud tops, particularly in multilayer cloud situations. C-band radar and soundings during the Tropical Ocean and Global Atmosphere (TOGA) Coupled Ocean–Atmosphere Response Experiment (COARE) also documented the transition from shallow to congestus to deep convective clouds and the concurrent moistening of the lower troposphere during the MJO developing phase (Lin and Johnson 1996; Johnson et al. 1999; Haertel et al. 2008), although C-band too typically underestimates the actual cloud top (Frederick and Schumacher 2008; Wu et al. 2009).

In this paper, we take advantage of the unique active remote sensing capabilities of the *CloudSat* (Stephens et al. 2008) and the Cloud–Aerosol Lidar and Infrared Pathfinder Satellite Observations (CALIPSO) (Winker et al. 2009) satellites, together with the precipitation and water vapor products from the *Aqua* Advanced Microwave Scanning Radiometer for Earth Observing System (EOS) (AMSR-E) instrument flying in formation with these satellites in the National Aeronautics and Space Administration (NASA) ''A-train'' constellation. Our goals are to directly document the depths of convective clouds occurring during the transition from the suppressed to the disturbed phase of the MJO and their relationship to humidity, to compare these to passive remote sensing views of the same phenomenon, and to evaluate the ability of a climate GCM to simulate these relationships. Our work builds on a recent *CloudSat* analysis of cloud-type behavior during the MJO by Riley et al. (2011). Section 2 describes the cloud, precipitation, and water vapor data used in our study as well as our technique for defining MJO events from reanalysis-based indices. Section 3 looks at the composite vertical cloud structure of the MJO in different

regions and how the transition from shallow to deep convection depends on column water vapor. Section 4 documents similar relationships in the ISCCP dataset with a specific focus on how ISCCP identifies scenes dominated by congestus clouds in the *CloudSat*/CALIPSO data. Section 5 performs a similar analysis with an experimental version of the Goddard Institute for Space Studies (GISS) GCM to gain insight into the performance of its convective entrainment parameterization. We summarize our results and discuss their implications in section 6.

2. Data and methods

Our analysis is based on cloud-base and -top detections by the *CloudSat* Cloud Profiling Radar (CPR) and CALIPSO Cloud–Aerosol Lidar with Orthogonal Polarization (CALIOP) lidar. The 2B Radar-Lidar Geometrical Profile Product (2B-GEOPROF-lidar) combines the two datasets to produce a single cloud mask product with ~1.4 × 2.5 km cross-track and along-track resolution (Mace et al. 2009). The 2B-GEOPROF-lidar version P2_R04 dataset covers the period July 2006–May 2010; we use data from all boreal nonsummer months (September–May) between 5°N–10°S and 65°–170°E, following Benedict and Randall (2007).

Surface clutter affects the ability of the CPR to detect hydrometeors below ~1-km altitude, particularly in the two range bins below 0.5 km (Marchand et al. 2008). We therefore define a convective cloud in the GEOPROF-lidar dataset as any radar–lidar column with lowest cloud base between 0.5 and 2 km. The actual cloud base (including any rain that falls from it) may sometimes be lower than this but in many cases is indistinguishable from clutter, so that the first reported GEOPROF-lidar cloud base is at higher altitude. The altitude of the first echo top above this base is designated as the convective cloud-top height (CTH). In principle some of the shallowest of these clouds might be stratocumulus, but such clouds are rare in the tropical warm-pool region that is the subject of this study. Stratiform rain regions of mesoscale convective clusters may be incorrectly classified as convective clouds by our definition, but inspection of many individual images (see, e.g., Fig. 7 for examples) and previous studies (Morita et al. 2006; Riley et al. 2011) indicate that organized convection is infrequent in the MJO shallow–deep convection transition region. Our CTH is the height at which a continuous echo starting from a low cloud base terminates, with no clear layers in between, so it does not include cirrus, anvils, or altostratus whose bases are well above the boundary layer. We have chosen not to use the *CloudSat* cloud classification (CLDCLASS) data product or any radar reflectivity criteria because cumulus congestus clouds do not fall into any single class and because there are ambiguities in using reflectivity thresholds to define congestus (Casey et al. 2011).

Nearly coincident AMSR-E passive microwave surface rainfall rates and column water vapor (CWV) from the NASA *Aqua* satellite are derived from the algorithm of Wentz and Meissner (2000, 2007). The AMSR-E products from the nearest pixel along the *CloudSat* orbital track were obtained from the AMSR-AUX product that is accumulated by *CloudSat* as part of the 2C-Precipitation Column (2C-PRECIP-COLUMN) dataset.

We also use the ISCCP classification of weather states based on a *k*-means clustering algorithm applied to joint histograms of cloud-top pressure and cloud optical thickness within 2.5° × 2.5° boxes (Rossow et al. 2005) for the period January 2006–December 2007. The classification identifies six independent clusters that can loosely be identified as scenes dominated by deep convection, cirrostratus anvils, congestus–disorganized convection, isolated cirrus, shallow cumulus, and stratocumulus (in addition to clear-sky cases). In fact, the cloud-top pressure–optical thickness distributions for each cluster include a variety of retrieved cloud-top pressures, so the assigned names are intended to merely depict the dominant cloud type in each cluster rather than the exclusive occurrence of that cloud type.

MJO events in the data are defined using a two-step procedure. We first use the real-time multivariate MJO index of Wheeler and Hendon (2004), which is based on an empirical orthogonal function (EOF) analysis of 850- and 200-hPa zonal winds from the National Centers for Environmental Prediction (NCEP)-1 reanalysis or NCEP operational analysis and satellite outgoing longwave radiation, with annual and interannual components of variability removed. MJO events located in the Indian Ocean, Maritime Continent, or west Pacific (phase index 2–7) are identified as those with intensity index > 1 continuously for at least 15 days. Each identified event is then located more precisely in the National Oceanic and Atmospheric Administration (NOAA) Climate Prediction Center daily MJO indices, which are based on an extended EOF analysis of 200-hPa velocity potential at 10 longitudes (Xue et al. 2002). We search the NOAA time series for index 10 (70°E) and indices 1–5 (80°, 100°, 120°, 140°, and 160°E). For each MJO date and region identified with the Wheeler–Hendon index, we find the three lowest consecutive values of the closest in longitude NOAA index that are <-0.6 and for which at least one value is <-1. The midpoint of these values is designated the MJO peak. If one index value is <-2.2 (identified as a strong MJO by Tromeur and Rossow 2010), we select that date as the peak regardless of

whether it is or is not the midpoint of the lowest three consecutive values of the index. A total of 10 MJO events satisfy the above criteria during the *CloudSat*/CALIPSO era.

The MJO peak thus identified is defined as day 0 at the corresponding longitude. All *CloudSat*/CALIPSO data on this date that fall within the width of the given longitude band (±5° or ±10°) are accumulated, along with those for peaks identified in the other longitude bands at other times, to create a composite cloud frequency of occurrence profile for day 0. Cloud profiles for other dates are referenced by lag relative to day 0 in the same longitude band and accumulated in similar fashion to create a composite MJO structure as a function of time. Although the NOAA index uses daily data as input, the index value is only reported at pentad resolution, so we smooth all composite plots with a 5-day running mean.

3. MJO structure as seen by *CloudSat*/CALIPSO

Figure 1 (upper) shows the composite frequency of occurrence of all clouds (not just those identified as convective) for all MJO events in the domain as a function of altitude and time lag relative to the MJO peak. High clouds dominate, with maximum occurrence near 14 km but often extending higher. Peak high cloudiness occurs near the MJO peak and lasts for about 10 days after the peak, which is not surprising in light of observations showing a shift from deep convective first baroclinic to anvil-like second baroclinic mode heating during these time periods (Kiladis et al. 2005; Mapes et al. 2006).

Perhaps more surprising is the fact that high clouds are just as prevalent for 10–15 days in advance of the peak and that these are the highest clouds seen at any time in the composite, some of them penetrating to the stratosphere. This behavior is not anticipated in canonical pictures of composite MJO structure (e.g., Fig. 13 of Benedict and Randall 2007) but has been noted by Riley et al. (2011). It suggests that the troposphere, having just begun the transition from suppressed to disturbed conditions, is at its most unstable at these times, while after the peak more frequent upper-level anvil heating and downdraft cooling are beginning to stabilize the upper troposphere and boundary layer. MJO lapse rate composites (Kikuchi and Takayabu 2004) show that the highest tropopause heights occur during the developing stage, as do the highest rain-top heights and lightning as seen in Tropical Rainfall Measuring Mission data (Morita et al. 2006), consistent with this picture. The presence of significant (20%–30% occurrence) cloud throughout the troposphere below the high cloud peak at these times is consistent with an origin of some of

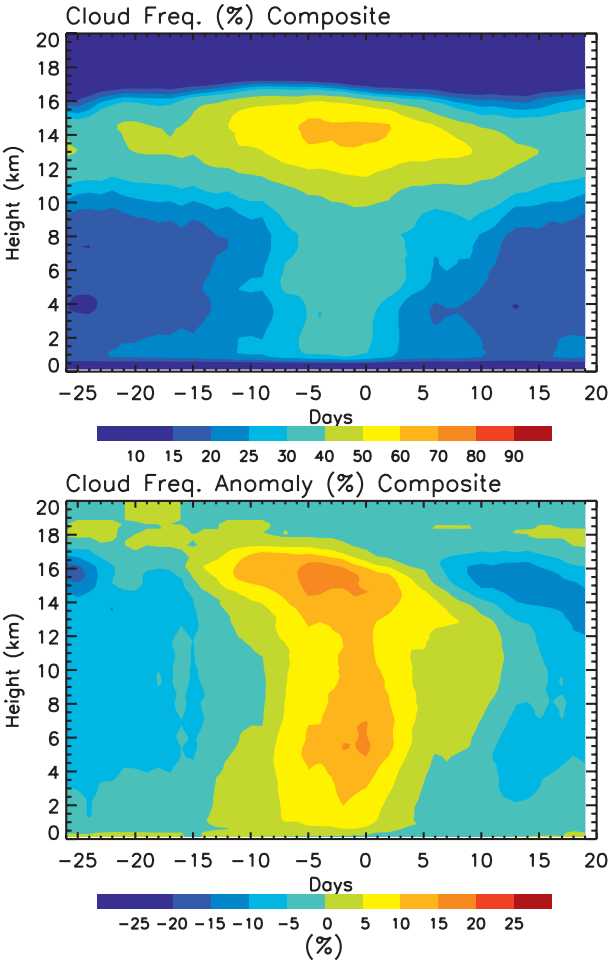

FIG. 1. MJO composite vertical profile of cloud frequency of occurrence vs lag relative to the peak for all 10 events in the domain in GEOPROF-lidar data. (top) Absolute occurrence frequencies and (bottom) anomaly relative to the longitudinal mean at each altitude.

these high clouds from deep convective detrainment. However, high clouds are fairly frequent (30%–50%) throughout the MJO life cycle including the most suppressed phases 2–3 weeks before and after the peak, when midtroposphere (4–8 km) cloudiness is at a minimum, suggesting that deep convection is infrequent then and thus that other proximate causes for the observed high cloud must also exist. Virts and Wallace (2010) suggest that this cloudiness is induced by motions associated with convectively generated eastward-propagating mixed Kelvin–Rossby waves.

Other features of the MJO, especially at lower altitudes, become more evident when we calculate anomalies of cloud occurrence relative to the time (in effect, longitude) mean (Fig. 1, lower). Shallow clouds with tops from ~0.5 to 4 km at −20 to −25 days gradually give way to deeper congestus with tops at ~4–6 km by day

−14, peaking near day −10, before the transition to deep convection occurs (Johnson et al. 1999; Haertel et al. 2008). Despite this general behavior, isolated deep convective clouds are also indicated by the weaker negative cloud cover anomalies at middle and upper levels from day −14 to −10 relative to the more suppressed phase. Thus a more accurate picture of the shift from suppressed to disturbed conditions in the MJO is not simply a transition from shallow to congestus to deep convection, but rather a shift in the relative frequency of occurrence of these cloud types, all of which occur sometimes in all phases (as also seen by Haertel et al. 2008). The anomaly plot also more clearly shows the transition to an anvil-dominated phase, with bases most frequent near 5 km and tops near 12–14 km, beginning 5 days after the peak and lasting for almost another week, after which a more bimodal cloud structure sets in. These features are generally similar to those seen for boreal summer intraseasonal variability in the altitude–latitude plane (Jiang et al. 2011).

The general picture of MJO cloud evolution seen by *CloudSat*/CALIPSO is very consistent with the "stretched building block" paradigm of Mapes et al. (2006). Mapes et al. envision the shallow convection–deep convection–anvil transition that takes place over the life cycle of an individual convective cluster to also describe tropical cloud evolution on time scales of days to weeks, with the relative frequency of occurrence of the three cloud "building blocks" varying on the longer time scale such that low-pass-filtered tropical cloud variability qualitatively resembles that on the individual cluster time scale.

Figure 2 shows similar anomaly composites for three individual regions: Indian Ocean (IO; 65°–110°E), Maritime Continent (MC; 110°–130°E), and west Pacific (WP; 130°–170°E). While the structure is generally similar in all three regions, there are also interesting differences: a more coherent anvil phase signature in the IO and generally more of the highest-altitude clouds near and before the MJO peak in the MC and especially the WP.

Figure 3 presents composites of precipitation (upper panel) and CWV (lower panel) for the entire domain and each subregion. CWV increases by a very modest ~5 mm over ~20 days in advance of the MJO peak (compared with precipitation rates that increase from ~5 to ~10 mm day^{-1}), that is, the "recharge" phase represents only a slight (a few percent) positive imbalance between the moisture convergence + evaporation source and the precipitation sink of moisture. Whether this can be explained solely by the interaction between convection and the humidity profile or whether temperature profile changes also come into play during this time is not known. The moisture budget appears to equilibrate about a week before the MJO peak while

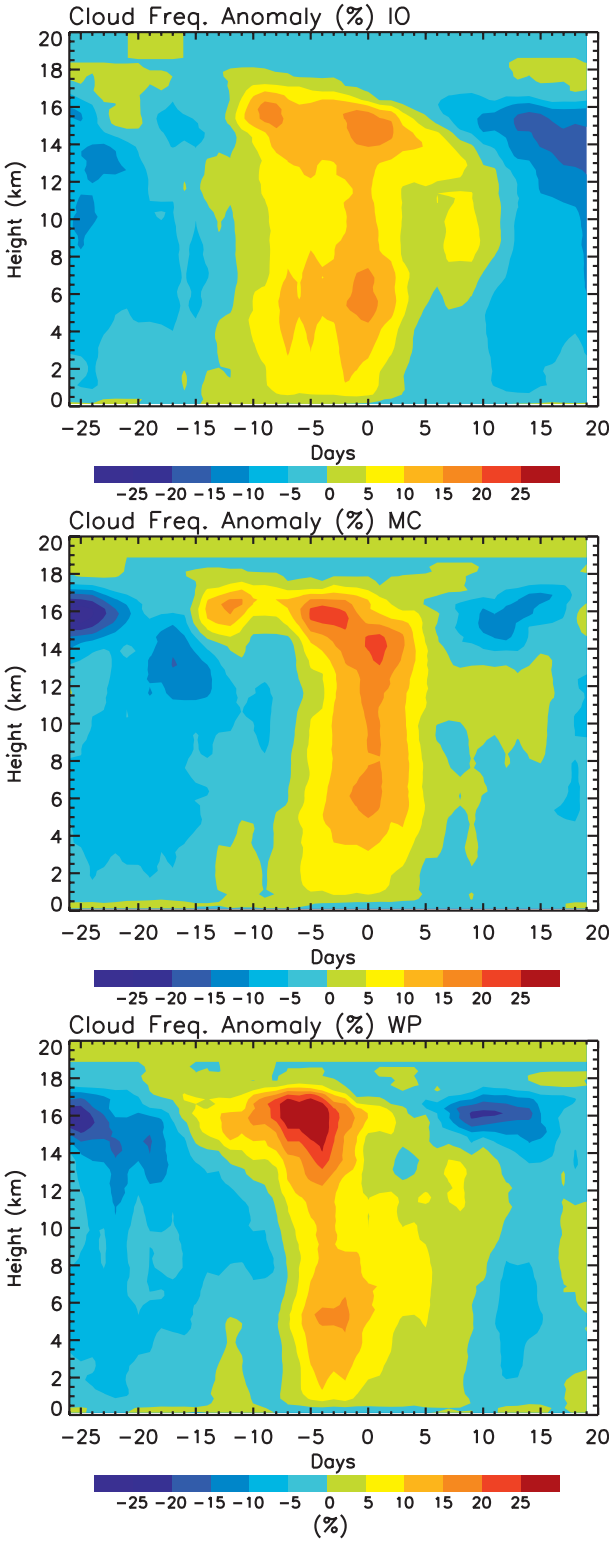

FIG. 2. As in (bottom) Fig. 1, but for the (top) IO, (middle) MC, and (bottom) WP.

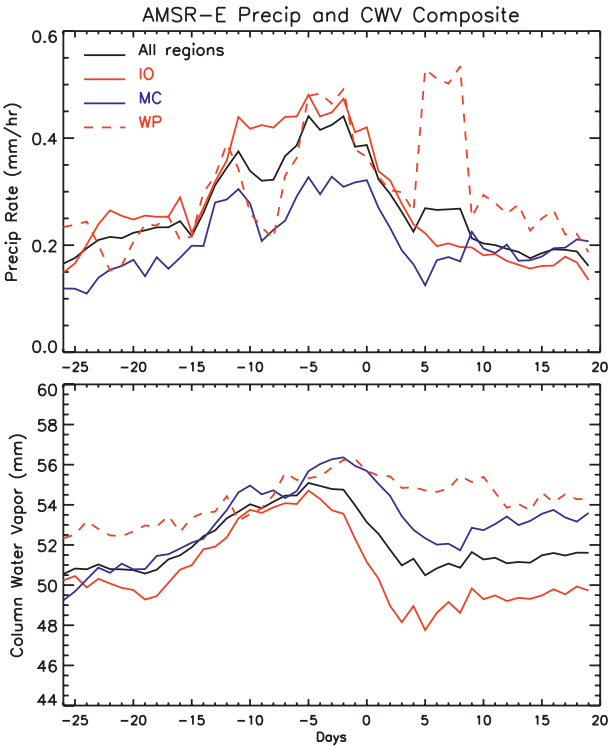

FIG. 3. MJO composites of AMSR-E (top) precipitation rate and (bottom) column water vapor vs lag for the entire domain and for the IO, MC, and WP subregions.

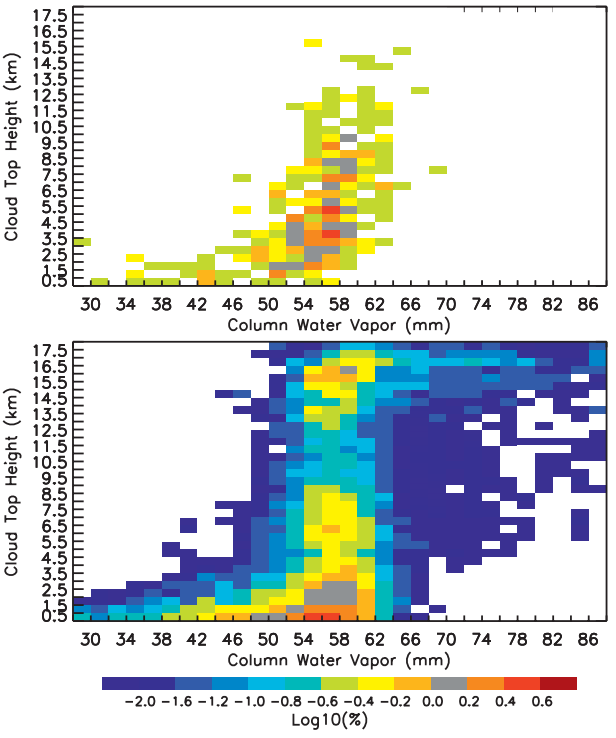

FIG. 4. Joint pdf of relative occurrence frequency (on a logarithmic scale) of convective cloud-top height and column water vapor for the MJO shallow–deep transition region (defined as lag −14 to lag −10 days). (top) Individual points in the pdf represent the 5°N–10°S mean convective cloud-top height and mean column water vapor for a given satellite pass through the region. (bottom) Individual points in the pdf represent single-satellite footprints containing a convective cloud.

precipitation continues to increase until ~2–3 days before the peak. After this there is a relatively rapid ''discharge'' phase lasting about a week, by whose end the atmosphere has returned to the suppressed phase and after which both precipitation and CWV remain steady for several weeks. The peak MJO precipitation anomaly is smallest in the MC, where the MJO is observed to weaken (e.g., Inness and Slingo 2006; Sobel et al. 2008). The discharge of water vapor is also weakest in the MC and strongest in the IO, the latter consistent with our impression from the cloud structure (Fig. 2) that the canonical MJO postpeak anvil phase is most obvious in the region in which it is most often triggered rather than downstream where it sometimes dissipates.

From this point forward we will focus attention on the cloud evolution during the shallow–deep transition phase in advance of the MJO peak, specifically the 5-day period from −14 days to −10 days in Figs. 1–3, which is of considerable interest as a challenge to GCM cumulus parameterizations. Precipitation over the tropical oceans is observed to ramp up sharply when CWV exceeds ~50 mm, associated with a strong increase in the relative humidity of the midtroposphere (Bretherton et al. 2004; Holloway and Neelin 2009). This should be associated with a systematic increase in the depth of convective clouds, a proposition that is directly testable with *CloudSat*/CALIPSO data using the convective CTH defined in section 2. (In principle our CTH identification might be compromised in the presence of tilted clouds, but the interested reader can look ahead to Fig. 7 to see that this is rarely an issue for the isolated convective cells that dominate the transition region.)

Figure 4 presents the joint probability density function (pdf) of CTH and CWV in the transition region, calculated in two different ways. To create the upper panel we calculated a mean CTH for all identified convective clouds in a single satellite pass through our domain (covering 15° of latitude and ~3° of longitude) and a corresponding mean CWV to represent a ''large-scale'' average that is as close as possible, given the effectively 2D nature of the *CloudSat*/CALIPSO curtain, to what a climate GCM's cumulus parameterization might try to predict instantaneously in a single grid box. Each such average contributes one point to the pdf, and occurrences are binned in intervals of 0.5 km and 2 mm to create the figure. For the lower panel we sampled the

single-footprint values of CTH and CWV for individual convective clouds to produce the true pdf at the cloud scale.

In both panels convective clouds are almost exclusively shallow for CWV $<$ 46 mm. Above 46 mm CTH rapidly ramps up to include congestus clouds and then frequent occurrences of deep clouds, but for 46 mm $<$ CWV $<$ 68 mm there is large variability in CTH with the most frequent cloud type still being shallow cumulus. The trimodal character of tropical convection (Johnson et al. 1999) is especially obvious in these conditions. The atmosphere spends most of its time in this transition CWV range. This behavior is very consistent with that observed for precipitation (Peters and Neelin 2006; Neelin et al. 2009); we will return to this issue in section 5. There are very few large-scale regions with mean CWV $>$ 68 mm, but numerous instances at the cloud scale. For these very high CWV values, convective clouds are primarily very deep, the majority having tops higher than 14 km. (Anvils do not contribute to this figure because of our requirement that cloud base be between 0.5 and 2 km.)

There is currently some controversy about the extent to which *CloudSat*/CALIPSO snapshots are capturing the actual ''terminal'' tops of congestus clouds as opposed to the tops of ''transient'' congestus that are still rising to become deep convection (Luo et al. 2009; Bacmeister and Stephens 2011; Casey et al. 2011). Resolution of this issue is important for the use of these data to evaluate GCM parameterizations, which simulate only the ''terminal'' cloud-top altitude. The behavior at very high CWV values in the lower panel of Fig. 4 is inconsistent with a large contribution from transient convection, since a large transient population would produce a variety of instantaneous cloud depths, representing different stages of ascent, of comparable probability of occurrence in the very humid conditions in which deep convection dominates. Apparently deep convection in the tropics sustains itself near its equilibrium level for a much longer time than the time it takes a given parcel to ascend to cloud top. We therefore conclude that the large CTH variability at intermediate CWV values is a mostly accurate reflection of the actual distribution of convective cloud-top heights.

4. ISCCP portrayal of the shallow–deep convection transition

CloudSat and CALIPSO provide the most authoritative global picture of cloud locations and depths in existence because of their unique active remote sensing capabilities. The limitation of active sensing, however, is spatial and temporal coverage. GEOPROF-lidar data ''curtains'' are in effect a series of two-dimensional slices through the atmosphere, meaning that each individual location on earth is sampled very infrequently. Furthermore, GEOPROF-lidar spans only 5 years at the present time, and recent difficulties with the *CloudSat* spacecraft batteries suggest that the dataset is unlikely to extend more than several years beyond this.

One important function of *CloudSat*/CALIPSO, therefore, is the perspective it can give us on the much more comprehensive and longer global records of cloudiness from passive remote sensing instruments. ISCCP, for example, provides an almost-global 3-hourly record of cloud properties spanning almost three decades and thus potentially has the ability to document longer-term dynamical variability in clouds. However, the ISCCP retrieval algorithm, based on reflected sunlight and emitted longwave radiation, is limited in its ability to accurately define cloud top, especially in multilayer cloud scenes and when clouds are thin or do not fill the satellite footprint (e.g., Chen and Del Genio 2009; Mace et al. 2011; Pincus et al. 2012).

Of particular interest for our purposes is the *k*-means clustering classification of cloud regimes, or ''weather states,'' that has been performed for most of the ISCCP record (Rossow et al. 2005). Each cluster represents preferred groupings of cloud-top pressure and optical thickness values that in principle can be used to isolate convection of different depths and distinguish convective from stratiform cloud types. Here, we examine the extent to which ISCCP captures the features of cloud variability during the MJO seen in *CloudSat*/CALIPSO data.

Chen and Del Genio (2009) and Tromeur and Rossow (2010) have already created composites of the relative frequency of occurrence of the different ISCCP cloud regimes as a function of MJO phase (Fig. 5). Comparison of this composite with the GEOPROF-lidar version in Fig. 1 indicates that in a climatological sense, ISCCP is very skillful in detecting both obvious and subtle characteristics of the MJO cloud structure. ISCCP not surprisingly captures the increase in occurrence of deep convective and cirrostratus anvils leading up to the MJO peak, and the greater dominance of the anvil cloud type just after the MJO peak; these features, associated with high optically thick clouds, are the most straightforward for visible–IR techniques to detect (e.g., Fu et al. 1990). Of more interest is that ISCCP portrays the suppressed-disturbed transition phase of the MJO as a decrease in the relative frequency of occurrence of shallow cumulus and congestus–disorganized convection, but with some deep convection present as well, rather than as a simple

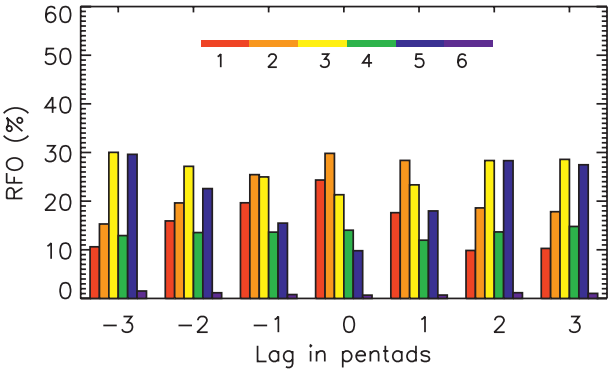

FIG. 5. Relative frequency of occurrence of ISCCP weather states as a function of lag relative to the MJO peak. The classification is as follows: 1 (red) = deep convective; 2 (orange) = anvil; 3 (yellow) = congestus–disorganized convection; 4 (green) = isolated thin cirrus; 5 (blue) = shallow cumulus; and 6 (violet) = marine stratocumulus. [Reprinted from Chen and Del Genio (2009) with permission from Springer.]

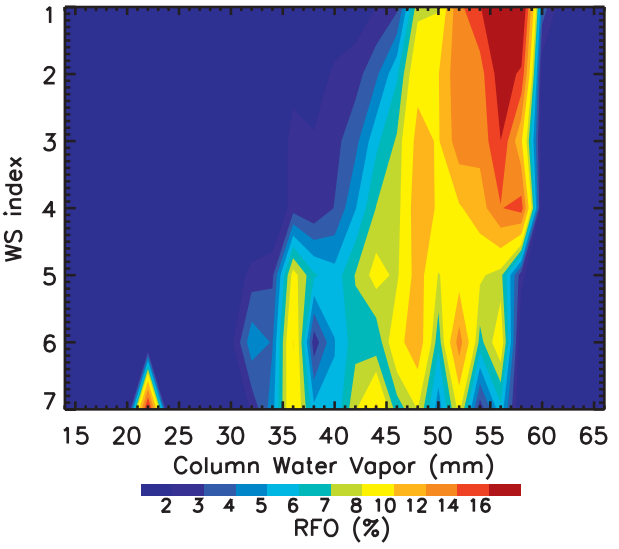

FIG. 6. Relative frequency of occurrence of ISCCP weather states vs AMSR-E monthly mean column water vapor for 15°N–15°S and 40°E–180°. States 1–6 as in Fig. 5; state 7 = clear sky.

change from shallow to congestus to deep clouds. The ISCCP congestus–disorganized convection peak is at −15 days, slightly earlier than seen by GEOPROF-lidar but consistent with TOGA COARE data (Haertel et al. 2008). Furthermore, ISCCP also detects the thin cirrus regime to be present at all times at roughly constant frequency of occurrence, similar to the impression from *CloudSat*/CALIPSO. This suggests that other non-convective large-scale processes must operate fairly regularly in the upper troposphere to supersaturate moist air.

Figure 6 shows the monthly mean relative frequency of occurrence of the ISCCP cloud regimes as a function of CWV. Comparison with the upper panel of Fig. 4 suggests generally good agreement with *CloudSat*/CALIPSO. For CWV $<$ 40 mm ISCCP detects shallow cumulus and stratocumulus almost exclusively, with only a small number of occurrences of the congestus–disorganized cloud type, consistent with GEOPROF-lidar. Deep convective and anvil clouds begin to appear at CWV 40 $\sim$ 45 mm, become comparable in occurrence to the shallow–congestus–disorganized types at CWV 45 $\sim$ 50 mm, and are the dominant cloud types for CWV $>$ 50 mm. *CloudSat*/CALIPSO indicate that shallow and deep convective cloud types do not occur with comparable frequency until CWV reaches 54–62 mm, and that deep convection only dominates for CWV $>$ 62 mm. However, the ISCCP plot is for monthly means rather than the instantaneous data used to construct the GEOPROF-lidar plot. Bretherton et al. (2004) show that the transition from light to heavy precipitation also occurs at smaller CWV values in monthly mean data relative to daily data.

A different perspective is obtained by examining the ISCCP cloud regime classification for individual *CloudSat*/CALIPSO satellite segments. Figure 7 shows eight examples of the GEOPROF-lidar cloud mask for satellite passes through the MJO shallow–deep transition phase region (days −14 to −10). These examples were randomly chosen from the subset of cases with numerous instances of cumulus congestus clouds, since the ISCCP congestus–disorganized convection regime is perhaps the least understood, is ostensibly a mix of cloud types and is therefore perhaps its greatest retrieval challenge. Beneath each image is the ISCCP cluster classification number (defined in Fig. 5) for each segment. Each satellite pass spans latitudes 5°N–10°S and covers 3°–4° of longitude and thus typically intersects six ISCCP 2.5° boxes.

Among all images we inspected we found no cases of purely congestus clouds over an area this large, though there are a few examples of mostly or exclusively congestus clouds in individual 2.5° segments, for example, the third segment on 15 February 2007 (first row, left panel) and the first segment on 21 December 2006 (second row, right panel). Keeping in mind that (i) *CloudSat*/CALIPSO samples only a small portion of an ISCCP gridbox and (ii) assigning a dominant cloud type visually is subjective when more than one type exists, it appears from the figure that when actual congestus are present, ISCCP correctly detects the congestus–disorganized type (regime 3) ~50% of the time. In cases where it does not, the culprit is often the ambiguity produced by near-ubiquitous cirrus that exist above lower-level clouds, which can either cause ISCCP to identify congestus beneath cirrus as shallow cumulus,

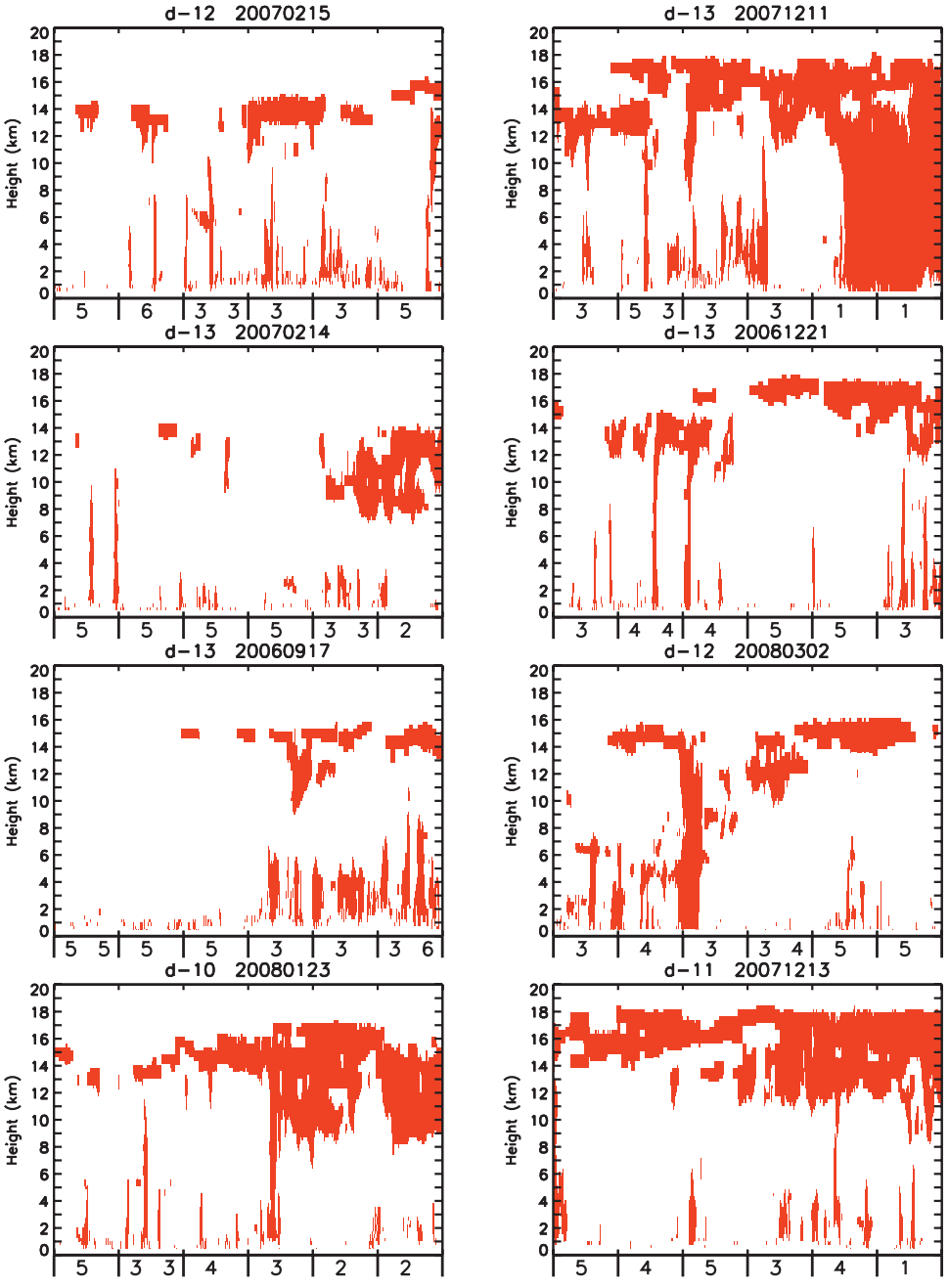

FIG. 7. Samples of the GEOPROF-lidar cloud mask between 5°N and 10°S for individual *CloudSat*/CALIPSO satellite passes through the MJO shallow–deep transition region that contains congestus clouds. The numbers underneath each image indicate the corresponding ISCCP weather state classification for each segment.

as on 2 March 2008 (third row, right panel, fifth segment), or as deep convection, as on 13 December 2007 (fourth row, right panel, sixth segment). On the other hand, one scene on 23 January 2008 with extensive cirrus and a single deep convective cell is classified as congestus–disorganized instead (fourth row, left panel, fourth segment).

5. GISS GCM simulation of the shallow–deep convection transition

The simulations described in this paper were conducted with the GISS Model E2 (GISS-E2) GCM (G. Schmidt et al. 2012, unpublished manuscript) at a resolution of 2° × 2.5° with 40 levels in the vertical . This

model version is almost identical to that used for the fifth Coupled Model Intercomparison Project. Model E2 uses a mass flux cumulus parameterization with a cloud-base neutral buoyancy closure, a division of the mass flux into two plumes with different entrainment rates, a representation of convective downdrafts, and a diagnostic updraft speed (Del Genio et al. 2007) that interactively determines condensate detrainment into an anvil based on empirical fall speeds applied to an assumed Marshall–Palmer size distribution (Del Genio et al. 2005).

Two features of the Model E2 cumulus parameterization are especially relevant to the discussion here. First, convective entrainment and updraft speed are diagnosed using the parameterization of Gregory (2001), as described in Del Genio et al. (2007). The Gregory scheme parameterizes the entrainment rate as $\varepsilon(z) = CB/w_c^2$, where B is the updraft parcel buoyancy, w_c is the updraft vertical velocity, and C is a constant representing the fraction of the buoyant turbulent kinetic energy generation used by entrainment. Del Genio and Wu (2010) have shown that the Gregory scheme is consistent with cloud-resolving model inferences of entrainment rate. Gregory suggests that C should be larger for shallow convection than deep convection; in Model E2 we set $C = 0.3$ and 0.6 for the two plumes that share the cumulus mass flux. The second relevant feature of Model E2 is its representation of convective precipitation evaporation. We assume that all precipitating condensate evaporates to the extent possible within the convective downdraft; the only evaporation into the environment occurs below cloud base. Convective moistening of the environment above cloud base thus only occurs at the cloud-top detrainment level.

Kim et al. (2011) have shown that the standard Model E2 does not have any MJO-like behavior. They conducted several sensitivity tests, finding three parameterization changes that helped produce a reasonable MJO-like signal in the model: 1) increasing the Gregory entrainment coefficient of the first convective plume from 0.3 to 0.6; 2) removing a limit on the mass of the convecting parcel that restricted it to no more than the mass of the cloud-base layer, which had led to occasional zero entrainment rates at upper levels; and 3) allowing only half the convective precipitating condensate to enter the downdraft and allowing the other half to evaporate into the environment. Standard diagnostics of MJO vertical structure and phase relationships for this version of the GCM can be found in Kim et al. (2011).

Unfortunately these changes produced several other undesirable results, including a drastic reduction of the downdraft mass flux, an overly strong Hadley cell, increased mean precipitation and precipitation variance, and radiation imbalance. We therefore made several additional changes to improve the model mean climate while preserving the MJO signal: 1) downdraft buoyancy was changed to include the effects of water vapor and condensate loading; 2) the entrainment coefficient C for the first convective plume was increased only to 0.4; and 3) stratiform cloud formation relative humidity thresholds were changed to bring the model to radiation balance.

This model version restores a vigorous downdraft and slightly improves the mean precipitation and precipitation variance, at the expense of a slightly weaker MJO signal. However, we regard this experimental model version as the best combination of mean state and MJO variability we have achieved to date, and we therefore focus on this simulation in this section. Figure 8 shows a Hovmöller diagram of outgoing longwave radiation for the equatorial region from the IO to the WP. Several MJO events are present in the experimental run, most notably a disturbance that is initiated in the Indian Ocean in late January and propagates eastward at $\sim$5 m s^{-1}, reaching the date line in mid-March.

Figure 9 shows the response of convection to the parameterization changes. Relative to the Model E2 control run, the experimental version has greater cumulus mass flux (left panel) in the lower troposphere and slightly less in the upper troposphere, a result of increased entrainment. Convective heating (middle panel) and drying (right panel) are reduced in the middle troposphere despite the increased mass flux there, due to the increased rain evaporation. This behavior suggests that the experimental model version allows tropospheric moisture to build during shallower phases of convection, perhaps favoring the production of ''moisture modes'' as portrayed in simple models of the MJO (e.g., Raymond et al. 2009) and perhaps seen in other GCMs (Hannah and Maloney 2011).

To further investigate the model's convection–humidity relationship, Fig. 10 shows the composite relative humidity profile as a function of precipitation for the control run (upper), the experimental version (middle), and the difference between the two (lower). Several previous modeling studies have argued that a sharp transition from a dry middle troposphere at weak rain rates to a very humid middle troposphere at high rain rates is diagnostic of a good MJO simulation (Thayer-Calder and Randall 2009; Zhu et al. 2009), though this is not the case for every model (Kim et al. 2011a). The GISS model behavior is consistent with the idea that a strong contrast in midlevel humidity between light and heavy rain situations is diagnostic of a good MJO. Stronger entrainment in the experimental version produces a drier middle–upper troposphere relative to the control for all but the strongest rain rates, while

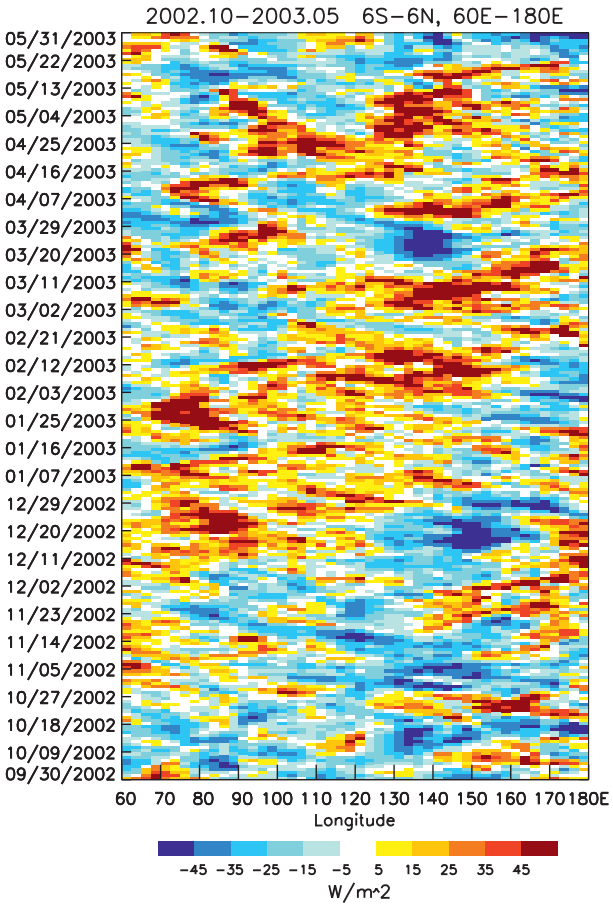

FIG. 8. Hovmöller diagram of outgoing longwave radiation anomalies for the equatorial 60°E–180° region for October–May for the GCM experimental version. Positive anomalies indicate more high, thick clouds.

increased rain evaporation moistens the middle–lower troposphere, especially in heavily raining locations where the experiment's relative humidity is 20%–25% wetter than the control. A similar sensitivity to entrainment and rain evaporation was shown by Hannah and Maloney (2011).

Since the experimental GCM version simulates an MJO, it is of interest to examine its transition from shallow to deep convection more closely. We therefore created a GCM analog of the *CloudSat*/CALIPSO joint distribution of CTH and CWV for the MJO transition region (Fig. 11). (The closest comparison should be with the upper panel of Fig. 4, in which the data are averaged over a large scale more comparable to a GCM gridbox.) Both the more weakly entraining (Plume 1, upper panel) and more strongly entraining (Plume 2, lower panel) plumes exhibit a gradual transition from shallow to deep convection as CWV increases. For Plume 1 the transition occurs too soon, at CWV 44 ~ 46 mm as opposed to the observed CWV ~50 mm. For Plume 2, however, the behavior better resembles that observed, with a shallow–deep transition at 50 ~ 54 mm. (Note that the observations in Fig. 4 are for ocean-only points, since AMSR-E CWV is only retrieved over ocean. Doing the same for the GCM would eliminate any contribution from the MC region, so instead Fig. 11 is plotted for grid boxes that are >50% ocean.) The GCM never produces values of CWV > 72 mm, as AMSR-E detects regularly on the individual footprint scale and even occasionally in the larger-scale mean, and so the GCM does not have a broad high-CWV regime of almost exclusively deep convection, at least in the MJO shallow–deep transition region, as is seen by *CloudSat*/CALIPSO.

Figure 4 raises the question of why the atmosphere produces both shallow and deep convection for CWV 54 ~ 62 mm. This has been discussed extensively in the context of the maximum observed variance of precipitation at intermediate values of CWV. Among the mechanisms proposed are self-organized criticality as occurs in continuous phase transitions (Neelin et al. 2009), a threshold boundary layer water vapor value for precipitation combined with independently varying boundary layer and free troposphere humidity (Muller et al. 2009), and stochastic triggers for deep convection (Stechmann and Neelin 2012). All of these ideas have features in common, most notably an emphasis on water vapor as the controlling factor for convection depth.

We cannot answer this question in the *CloudSat*/CALIPSO observations, since they are not accompanied by soundings, but we can address it in the GCM. The GISS cumulus parameterization has no explicit stochastic elements, yet it nonetheless produces the full range of observed CTH variability for a given CWV. To examine the reasons for this we defined two subsets of the Plume 2 convective events that fall within a narrow range of CWV values (55.5–56 mm), one consisting of shallow convective clouds (CTH < 3 km) and the other deep convective clouds (CTH > 9 km). The mean environmental (gridbox mean) moist static energy and saturation moist static energy profiles for these subsets prior to each convective event are shown in Fig. 12. The deep convective subset has slightly higher relative humidity at most levels and a lower lifting condensation level, mostly because of slightly cooler temperatures. Specific humidity is similar for shallow and deep events in the boundary layer and slightly drier for the deep subset in the middle troposphere, but slightly wetter in the upper troposphere. Similar behavior exists for other narrow ranges of CWV between 46 and 60 mm. The GCM deep convective subset also has a slightly steeper free-troposphere lapse rate than the shallow subset.

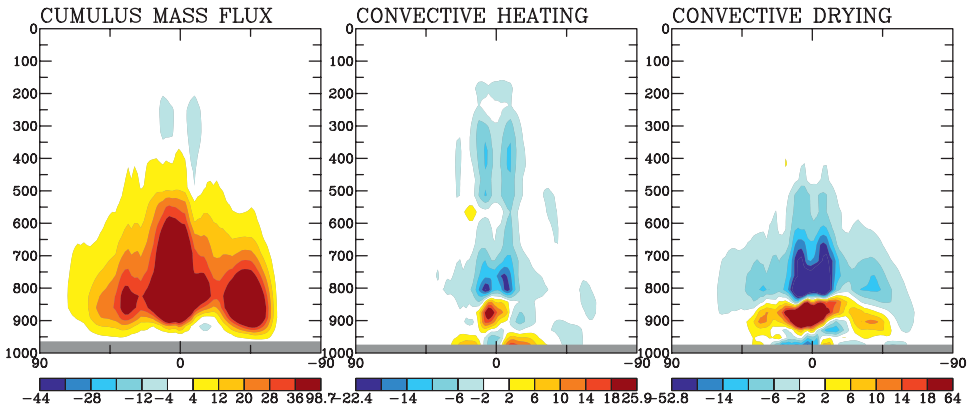

FIG. 9. Zonal mean vertical profiles of differences in (left) cumulus mass flux (10^{-5} hPa s^{-1}), (middle) convective heating (10^{-2} W m^{-2} hPa^{-1}), and (right) convective drying (10^{-2} W m^{-2} hPa^{-1}) for the GCM experiment minus control.

6. Discussion

The *CloudSat*/CALIPSO dataset provides an unprecedented opportunity to explicitly observe the vertical cloud structure associated with variations of convection during the MJO. The observed structure agrees qualitatively with previous indirect inferences, with shallow convection during the suppressed phase gradually giving way to congestus as the troposphere moistens, leading eventually to the onset of widespread deep convection as column water vapor peaks and then a further transition to a cloud structure dominated by upper-troposphere anvil clouds as moisture is discharged by precipitation and the suppressed phase returns. However, *CloudSat* and CALIPSO reveal or confirm a number of more subtle aspects of the MJO behavior: 1) the presence of convection of all depths during all phases, that is, the transitions are best described as gradual changes in the relative frequency of occurrence of different convection depths rather than a simple shallow–congestus–deep progression; 2) the almost ubiquitous presence of cirrus regardless of MJO phase, especially in the two weeks prior to the MJO peak; 3) the occurrence of the deepest, tropopause-penetrating convective events at the onset of the disturbed phase a week before the MJO peak; and 4) regional differences in MJO structure, with the most canonical variations of structure with MJO phase occurring in the Indian Ocean where many MJO events are triggered. Convective cloud-top height variations with column water vapor during the shallow–deep transition phase are consistent with previously documented precipitation variations—a transition from shallow to deep beginning at CWV ~ 46 mm and occurrence of the full range of convection depths when CWV ~50–65 mm.

ISCCP weather state occurrences exhibit behavior as a function of MJO phase and CWV that is generally consistent with the *CloudSat*/CALIPSO data, including some of the subtle features described above. This suggests that despite the limitations of passive remote sensing, the almost three-decade span of the ISCCP dataset can be a valuable source of information on decadal climatological variations in vertical cloud structure. Instantaneously, though, the ISCCP weather state classification appears to correctly identify congestus-dominated scenes only about half the time, primarily because of the frequently occurring cirrus that overlay congestus clouds. Thus it appears (to the extent that the small sample examined here is representative) that the ISCCP classification may somewhat underrepresent the occurrence of congestus, at least in the tropical warm-pool region where cirrus occur most frequently. The problem may be less severe in other geographic regions that contain fewer cirrus.

An experimental version of the GISS GCM cumulus parameterization with increased entrainment and rain evaporation that produces MJO-like variability performs surprisingly well in simulating variations of convective cloud-top height with column water vapor. The parameterization partitions the cumulus mass flux into two plumes with weaker and stronger entrainment, intended to allow for the possibility of simultaneous deep and shallow (or congestus) convection in a grid box without invoking a separate shallow convection parameterization. The more weakly entraining plume transitions from shallow to deep convection at CWV values lower than observed, while the more strongly entraining plume simulates the transition at approximately the correct value of CWV.

Kim et al. (2011) show that a good simulation of the MJO can be obtained using only the more strongly

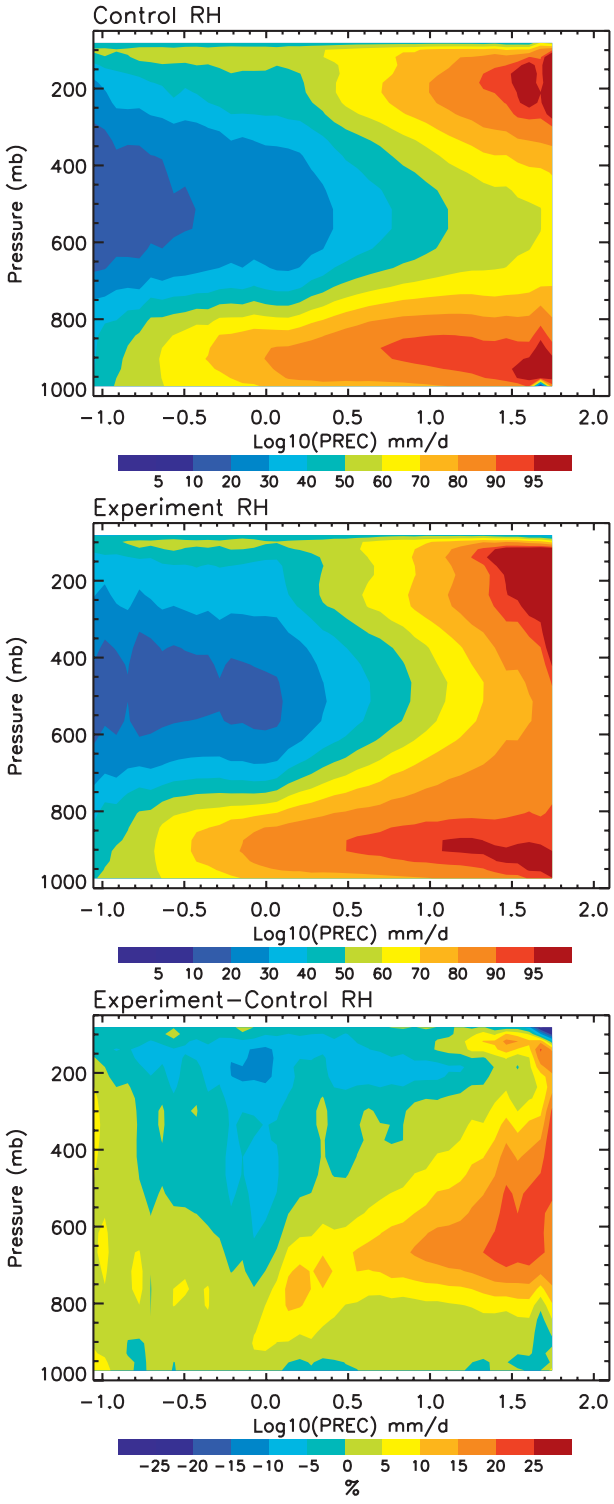

FIG. 10. Composite vertical profiles of relative humidity vs precipitation for the MJO region for the (top) GCM control run, (middle) GCM experiment, and (bottom) difference between the two.

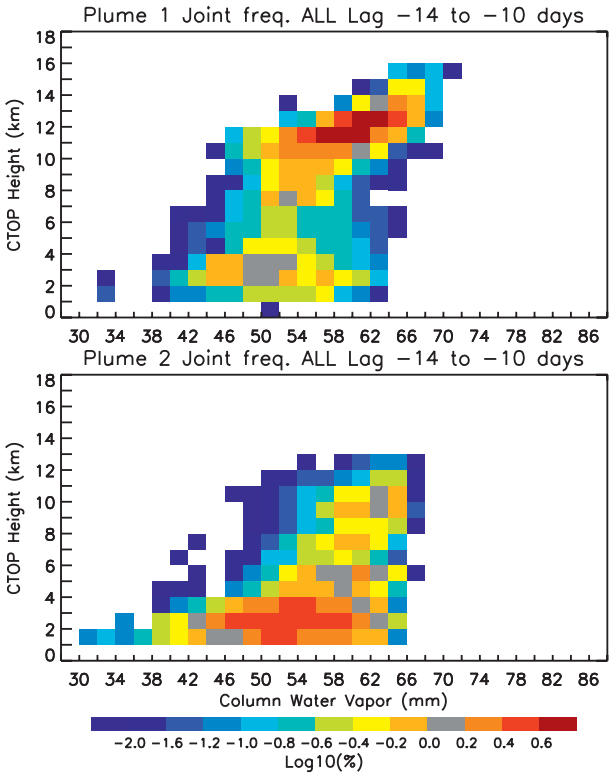

FIG. 11. As in Fig. 4, but for the (top) less-entraining and (bottom) more-entraining convective plume in the GCM experiment. For this figure the transition region is defined as the 10–14-day period prior to the peak positive outgoing longwave radiation anomaly for the MJO event in Fig. 8 discussed in the text.

entraining plume. However, there are indications that such a model suppresses stronger convective events, thus arguing for weaker entrainment under the right circumstances. (For example, comparing Figs. 4 and 11, we can see that the more weakly entraining plume simulates peak CTH values of 14–16 km, similar to the spatially averaged observations, while the strongly entraining plumes never penetrate beyond 12–13 km.) The failure of the more weakly entraining plume to simulate the shallow–deep transition at the correct CWV value suggests therefore that weaker entrainment must be restricted to special (specifically, wetter) conditions not anticipated by the current parameterization. Such linkages have been proposed elsewhere (Bechtold et al. 2008; Mapes and Neale 2011).

In the current model the part of the cumulus mass flux assigned to Plume 1 is determined by the grid-scale low-level convergence; the remainder of the mass flux required to create neutral cloud-base buoyancy goes into Plume 2. Kikuchi and Takayabu (2004) show that strong low-level convergence exists even in the suppressed–developing stage of the MJO, as well as near the MJO

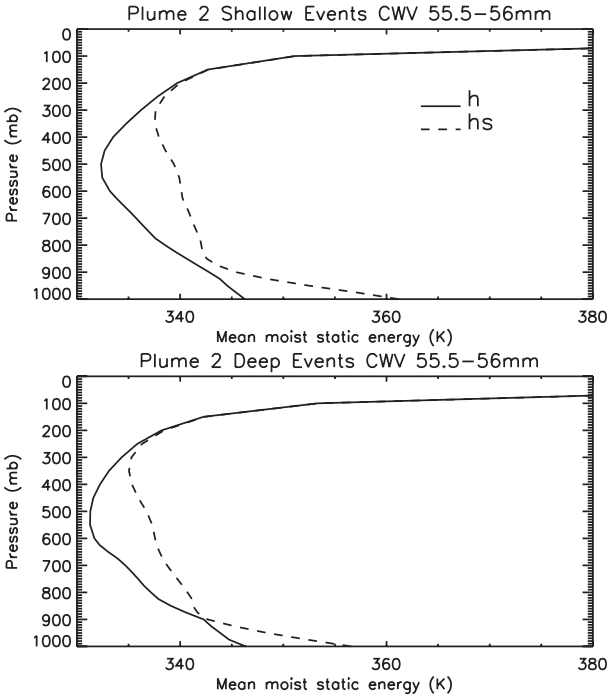

FIG. 12. Moist static energy (h, solid) and saturation moist static energy (h_s, dashed) profiles for (top) shallow (<3 km) and (bottom) deep (>9 km) CTH subsets of GCM strongly entraining convective clouds for $55.5 < \text{CWV} < 56$ mm.

peak. Thus, if entrainment rate variations in part distinguish the shallow–developing stage from the peak stage, low-level convergence on GCM grid scales is not a good discriminator. Cloud-resolving model simulations indicate instead that mesoscale convergence at the gust front formed by the spreading of downdraft-generated boundary layer cold pools is associated with the weaker entrainment characteristic of deep convection (Kuang and Bretherton 2006; Khairoutdinov and Randall 2006; Del Genio and Wu 2010). Thus, an improved parameterization might restrict the occurrence of Plume 1 to situations after the onset of deep convection and after downdraft cold pools had already occurred. Ideally it would produce less frequent deep convection when CWV < 50 mm and slightly more (and deeper) deep convection when CWV > 50 mm because Plume 1 would have a nonzero mass flux only when the column was sufficiently moist to have already triggered deep convection.

Proposed mechanisms for the variability of precipitation and convection depth at intermediate CWV values in one way or another invoke stochastic aspects of convection associated with variations in the water vapor field. The spatial scale on which such variability occurs is not always specified, but it is often assumed for the purposes of GCM cumulus parameterizations that subgrid-scale variability, especially of boundary layer humidity, is the source of the stochastic convective response to a given thermodynamic state (e.g., Plant and Craig 2008; Tompkins and Berner 2008). Such variability undoubtedly exists (perhaps in Fig. 7) and is worth attempting to parameterize. However, our results show that in principle it is possible to produce the full range of variability of convective depths at a given CWV value in a deterministic cumulus parameterization as a result of small variations in boundary layer and free troposphere relative humidity at the GCM grid scale and as a result of small temperature and lapse rate variations as well. Such variability might be associated with synoptic tropospheric dry air intrusions from the subtropics (Mapes and Zuidema 1996; Yoneyama and Parsons 1999) and/or small short-term departures from strict quasi equilibrium following prior convective events. Kuang (2010) and Tulich and Mapes (2010) have independently shown that in a cloud-resolving model, small perturbations of both moisture and temperature can affect convection depth, especially when the perturbation occurs at low altitude. Consistent with this, the GISS GCM produces deeper convection when the boundary layer is slightly more humid, though the free troposphere also plays a role (Fig. 12). It may also be relevant to the question of why the deepest convection during the MJO actually occurs during its developing phase (Fig. 1) rather than near the MJO peak, even sometimes at intermediate local CWV values (Fig. 4, lower panel). Such events would appear to be a good test for GCM entrainment parameterizations (e.g., Mapes and Bacmeister 2012).

The *CloudSat*/CALIPSO data are not accompanied by tropical ocean soundings and thus cannot answer this question by themselves. However, as part of the Dynamics of the MJO (DYNAMO) Indian Ocean field experiment beginning in late 2011, a variety of scanning radars will be deployed to map not only the three-dimensional cloud field but also water vapor in the vicinity of the clouds, along with enhanced soundings of the environment. Observations such as these should provide further insight into the processes that trigger the disturbed phase of the MJO and the features absent from current cumulus parameterizations that limit our ability to simulate it.

Acknowledgments. The authors thank Brian Mapes and two anonymous reviewers for constructive comments that helped improve the manuscript. This research was supported by the NASA *CloudSat*/CALIPSO and Precipitation Measurement Missions and the NASA Modeling and Analysis Program. DK was supported by NASA Grant NNX09AK34G. Some of the ISCCP data products used in this paper were produced with support

from the American Recovery and Reinvestment Act as part of the Metrics for General Circulation Model Evaluation project (http://gcss-dime.giss.nasa.gov/ARRA/arra.html).

REFERENCES

Bacmeister, J. T., and G. L. Stephens, 2011: Spatial statistics of likely convective clouds in *CloudSat* data. *J. Geophys. Res.,* **116,** D04104, doi:10.1029/2010JD014444.

Bechtold, P., M. Köhler, T. Jung, F. Doblas-Reyes, M. Leutbecher, M. J. Rodwell, F. Vitart, and G. Balsamo, 2008: Advances in simulating atmospheric variability with the ECMWF model: From synoptic to decadal time-scales. *Quart. J. Roy. Meteor. Soc.,* **134,** 1337–1351.

Benedict, J. J., and D. A. Randall, 2007: Observed characteristics of the MJO relative to maximum rainfall. *J. Atmos. Sci.,* **64,** 2332–2354.

Bladé, I., and D. L. Hartmann, 1993: Tropical intraseasonal oscillations in a simple nonlinear model. *J. Atmos. Sci.,* **50,** 2922–2939.

Bretherton, C. S., M. E. Peters, and L. E. Back, 2004: Relationships between water vapor path and precipitation over the tropical oceans. *J. Climate,* **17,** 1517–1528.

Casey, S. P. F., E. J. Fetzer, and B. H. Kahn, 2011: Revised identification of tropical oceanic cumulus congestus as viewed by *CloudSat*. *Atmos. Chem. Phys. Discuss.,* **11,** 14 883–14 902.

Chen, Y., and A. D. Del Genio, 2009: Evaluation of tropical cloud regimes in observations and a general circulation model. *Climate Dyn.,* **32,** 355–369.

Del Genio, A. D., and J. Wu, 2010: Entrainment and the diurnal cycle of continental convection. *J. Climate,* **23,** 2722–2738.

——, W. Kovari, M.-S. Yao, and J. Jonas, 2005: Cumulus microphysics and climate sensitivity. *J. Climate,* **18,** 2376–2387.

——, M.-S. Yao, and J. Jonas, 2007: Will moist convection be stronger in a warmer climate? *Geophys. Res. Lett.,* **34,** L16703, doi:10.1029/2007GL030525.

Derbyshire, S., I. Beau, P. Bechtold, J.-Y. Grandpeix, J.-M. Piriou, J.-L. Redelsperger, and P. M. M. Soares, 2004: Sensitivity of moist convection to environmental humidity. *Quart. J. Roy. Meteor. Soc.,* **130,** 3055–3079.

Frederick, K., and C. Schumacher, 2008: Anvil characteristics as seen by C-POL during the Tropical Warm Pool International Cloud Experiment (TWP-ICE). *Mon. Wea. Rev.,* **136,** 206–222.

Fu, R., A. D. Del Genio, and W. B. Rossow, 1990: Behavior of deep convective clouds in the tropical Pacific deduced from ISCCP radiances. *J. Climate,* **3,** 1129–1152.

Gregory, D., 2001: Estimation of entrainment rate in simple models of convective clouds. *Quart. J. Roy. Meteor. Soc.,* **127,** 53–72.

Haertel, P. T., G. N. Kiladis, A. Denno, and T. M. Rickenbach, 2008: Vertical-mode decompositions of 2-day waves and the Madden–Julian oscillation. *J. Atmos. Sci.,* **65,** 813–833.

Hannah, W. M., and E. D. Maloney, 2011: The role of moisture–convection feedbacks in simulating the Madden–Julian oscillation. *J. Climate,* **24,** 2754–2770.

Holloway, C. E., and J. D. Neelin, 2009: Moisture vertical structure, column water vapor, and tropical deep convection. *J. Atmos. Sci.,* **66,** 1665–1683.

Hu, Q., and D. A. Randall, 1994: Low-frequency oscillations in radiative–convective systems. *J. Atmos. Sci.,* **51,** 1089–1099.

Inness, P. M., and J. M. Slingo, 2006: The interaction of the Madden–Julian oscillation with the Maritime Continent in a GCM. *Quart. J. Roy. Meteor. Soc.,* **132,** 1645–1667.

Jensen, M. P., and A. D. Del Genio, 2006: Factors limiting convective cloud-top height at the ARM Nauru Island climate research facility. *J. Climate,* **19,** 2105–2117.

Jiang, X., D. E. Waliser, J.-L. Li, and C. Woods, 2011: Vertical cloud structures of the boreal summer intraseasonal variability based on *CloudSat* observations and ERA-Interim reanalysis. *Climate Dyn.,* **36,** 2219–2232.

Johnson, R. H., T. M. Rickenbach, S. A. Rutledge, P. E. Ciesielski, and W. H. Schubert, 1999: Trimodal characteristics of tropical convection. *J. Climate,* **12,** 2397–2418.

Kemball-Cook, S. R., and B. C. Weare, 2001: The onset of convection in the Madden–Julian oscillation. *J. Climate,* **14,** 780–793.

Khairoutdinov, M., and D. Randall, 2006: High-resolution simulation of shallow-to-deep convection transition over land. *J. Atmos. Sci.,* **63,** 3421–3436.

——, C. DeMott, and D. Randall, 2008: Evaluation of the simulated interannual and subseasonal variability in an AMIP-style simulation using the CSU multiscale modeling framework. *J. Climate,* **21,** 413–431.

Khouider, B., and A. J. Majda, 2006: A simple multicloud parameterization for convectively coupled tropical waves. Part I: Linear analysis. *J. Atmos. Sci.,* **63,** 1308–1323.

Kikuchi, K., and Y. N. Takayabu, 2004: The development of organized convection associated with the MJO during TOGA COARE IOP: Trimodal characteristics. *Geophys. Res. Lett.,* **31,** L10101, doi:10.1029/2004GL019601.

Kiladis, G. N., K. H. Straub, and P. T. Haertel, 2005: Zonal and vertical structure of the Madden–Julian oscillation. *J. Atmos. Sci.,* **62,** 2790–2809.

Kim, D., and Coauthors, 2009: Application of MJO diagnostics to climate models. *J. Climate,* **22,** 6413–6436.

——, A. H. Sobel, E. D. Maloney, D. M. W. Frierson, and I.-S. Kang, 2011: A systematic relationship between intraseasonal variability and mean state bias in AGCM simulations. *J. Climate,* **24,** 5506–5520.

Kuang, Z., 2008: A moisture–stratiform instability for convectively coupled waves. *J. Atmos. Sci.,* **65,** 834–854.

——, 2010: Linear response functions of a cumulus ensemble to temperature and moisture perturbations and implications for the dynamics of convectively coupled waves. *J. Atmos. Sci.,* **67,** 941–962.

——, and C. S. Bretherton, 2006: A mass-flux scheme view of a high-resolution simulation of a transition from shallow to deep cumulus convection. *J. Atmos. Sci.,* **63,** 1895–1909.

Lau, K.-M., and H.-T. Wu, 2010: Characteristics of precipitation, cloud, and latent heating associated with the Madden–Julian oscillation. *J. Climate,* **23,** 504–518.

Lin, J.-L., and Coauthors, 2006: Tropical instraseasonal variability in 14 IPCC AR4 climate models. Part I: Convective signals. *J. Climate,* **19,** 2665–2690.

Lin, X., and R. H. Johnson, 1996: Kinematic and thermodynamic characteristics of the flow over the western Pacific warm pool during TOGA COARE. *J. Atmos. Sci.,* **53,** 695–715.

Luo, Z. Z., G. Y. Liu, G. L. Stephens, and R. H. Johnson, 2009: Terminal vs. transient cumulus congestus: A *CloudSat* perspective. *Geophys. Res. Lett.,* **36,** L05808, doi:10.1029/2008GL036927.

Mace, G. G., Q. Zhang, M. Vaughan, R. Marchand, G. Stephens, C. Trepte, and D. Winker, 2009: A description of hydrometeor layer occurrence statistics derived from the first year of merged *CloudSat* and CALIPSO data. *J. Geophys. Res.,* **114,** D00A26, doi:10.1029/2007JD009755.

——, S. Houser, S. Benson, S. A. Klein, and Q. Min, 2011: Critical evaluation of the ISCCP simulator using ground-based remote sensing data. *J. Climate,* **24,** 1598–1612.

Madden, R., and P. Julian, 1971: Detection of a 40-50-day oscillation in the zonal wind in the tropical Pacific. *J. Atmos. Sci.,* **28,** 702–708.

Mapes, B. E., and P. Zuidema, 1996: Radiative-dynamical consequences of dry tongues in the tropical troposphere. *J. Atmos. Sci.,* **53,** 620–638.

——, and R. Neale, 2011: Parameterizing convective organization to escape the entrainment dilemma. *J. Adv. Model. Earth Syst.,* **3,** M06004, doi:10.1029/2011MS000042.

——, and J. T. Bacmeister, 2012: Diagnosis of tropical biases and the MJO from patterns in MERRA's analysis tendency fields. *J. Climate,* in press.

——, S. Tulich, J. Lin, and P. Zuidema, 2006: The mesoscale convection life cycle: Building block or prototype for large-scale tropical waves? *Dyn. Atmos. Oceans,* **42,** 3–29.

Marchand, R., G. G. Mace, T. Ackerman, and G. Stephens, 2008: Hydrometeor detection using *CloudSat*—An earth-orbiting 94-GHz cloud radar. *J. Atmos. Oceanic Technol.,* **25,** 519–533.

Morita, J., Y. N. Takayabu, S. Shige, and Y. Kodama, 2006: Analysis of rainfall characteristics of the Madden–Julian oscillation using TRMM satellite data. *Dyn. Atmos. Oceans,* **42,** 107–126.

Muller, C. J., L. E. Back, P. A. O'Gorman, and K. A. Emanuel, 2009: A model for the relationship between tropical precipitation and column water vapor. *Geophys. Res. Lett.,* **36,** L16804, doi:10.1029/2009GL039667.

Neelin, J. D., O. Peters, and K. Hales, 2009: The transition to strong convection. *J. Atmos. Sci.,* **66,** 2367–2384.

Peters, O., and J. D. Neelin, 2006: Critical phenomena in atmospheric precipitation. *Nat. Phys.,* **2,** 393–396.

Pincus, R., S. Platnick, S. A. Ackerman, R. S. Hemler and R. J. P. Hoffmann, 2012: Reconciling simulated and observed views of clouds: MODIS, ISCCP, and the limits of instrument simulators. *J. Climate,* in press.

Plant, R. S., and G. C. Craig, 2008: A stochastic parameterization for deep convection based on equilibrium statistics. *J. Atmos. Sci.,* **65,** 87–105.

Raymond, D. J., S. L. Sessions, A. H. Sobel, and Z. Fuchs, 2009: The mechanics of gross moist stability. *J. Adv. Model. Earth Syst.,* **1,** doi:10.3894/JAMES.2009.1.9.

Riley, E. M., B. E. Mapes, and S. N. Tulich, 2011: Clouds associated with the Madden–Julian oscillation: A new perspective from *CloudSat*. *J. Atmos. Sci.,* **68,** 3032–3051.

Rossow, W. B., G. Tselioudis, A. Polak, and C. Jakob, 2005: Tropical climate described as a distribution of weather states indicated by distinct mesoscale cloud property mixtures. *Geophys. Res. Lett.,* **32,** L21812, doi:10.1029/2005GL024584.

Slingo, J. M., and Coauthors, 1996: Intraseasonal oscillations in 15 atmospheric general circulation models: Results from an AMIP diagnostic subproject. *Climate Dyn.,* **12,** 325–357.

Sobel, A. H., E. D. Maloney, G. Bellon, and D. M. Frierson, 2008: The role of surface heat fluxes in tropical intraseasonal oscillations. *Nat. Geosci.,* **1,** 653–657.

Sperber, K. R., S. Gualdi, S. Legutke, and V. Gayler, 2005: The Madden–Julian oscillation in ECHAM4 coupled and uncoupled general circulation models. *Climate Dyn.,* **25,** 117–140.

Stechmann, S. N., and J. D. Neelin, 2012: A stochastic model for the transition to strong convection. *J. Atmos. Sci.,* **68,** 2955–2970.

Stephens, G. L., P. J. Webster, R. H. Johnson, R. Engelen, and T. L'Ecuyer, 2004: Observational evidence for the mutual regulation of the tropical hydrological cycle and tropical sea surface temperatures. *J. Climate,* **17,** 2213–2224.

——, and Coauthors, 2008: *CloudSat* mission: Performance and early science after the first 5 years of operation. *J. Geophys. Res.,* **113,** D00A18, doi:10.1029/2008JD009982.

Thayer-Calder, K., and D. A. Randall, 2009: The role of convective moistening in the Madden–Julian oscillation. *J. Atmos. Sci.,* **66,** 3297–3312.

Tian, B., D. E. Waliser, E. J. Fetzer, and Y. L. Yung, 2010: Vertical moist thermodynamic structure of the Madden–Julian oscillation in Atmospheric Infrared Sounder retrievals: An update and a comparison to ECMWF Interim reanalysis. *Mon. Wea. Rev.,* **138,** 4576–4582.

Tompkins, A. M., and J. Berner, 2008: A stochastic convective approach to account for model uncertainty due to unresolved humidity variability. *J. Geophys. Res.,* **113,** D18101, doi:10.1029/2007JD009284.

Tromeur, E., and W. B. Rossow, 2010: Interaction of tropical deep convection with the large-scale circulation in the MJO. *J. Climate,* **23,** 1837–1853.

Tulich, S. N., and B. E. Mapes, 2010: Transient environmental sensitivities of explicitly simulated tropical convection. *J. Atmos. Sci.,* **67,** 923–940.

Virts, K. S., and J. M. Wallace, 2010: Annual, interannual, and intraseasonal variability of tropical tropopause transition layer cirrus. *J. Atmos. Sci.,* **67,** 3097–3112.

Wentz, F. J., and T. Meissner, 2000: AMSR ocean algorithm. Remote Sensing Systems Algorithm Theoretical Basis Doc., version 2, 74 pp.

——, and ——, 2007: Supplement 1. Remote Sensing Systems Algorithm Theoretical Basis Doc., version 2, 6 pp.

Wheeler, M., and G. M. Kiladis, 1999: Convectively coupled equatorial waves: Analysis of clouds and temperature in the wavenumber-frequency domain. *J. Atmos. Sci.,* **56,** 374–399.

——, and H. Hendon, 2004: An all-season real-time multivariate MJO index: Development of an index for monitoring and prediction. *Mon. Wea. Rev.,* **132,** 1917–1932.

Winker, D. M., M. A. Vaughan, A. H. Omar, Y. Hu, K. A. Powell, Z. Liu, W. H. Hunt, and S. A. Young, 2009: Overview of the CALIPSO mission and CALIOP data processing algorithms. *J. Atmos. Oceanic Technol.,* **26,** 2310–2323.

Wu, J., A. D. Del Genio, M.-S. Yao, and A. B. Wolf, 2009: WRF and GISS SCM simulations of convective updraft properties during TWP-ICE. *J. Geophys. Res.,* **114,** D04206, doi:10.1029/2008JD010851.

Xue, Y., W. Higgins, and V. Kousky, 2002: Influences of the Madden Julian Oscillations on temperature and precipitation in North America during ENSO-neutral and weak ENSO winters. *Proc. Workshop on Prospects for Improved Forecasts of Weather and Short-Term Climate Variability on Subseasonal (2 Week to 2 Month) Time Scales,* Mitchellville, MD, NASA Goddard Space Flight Center, 4 pp.

Yoneyama, K., and D. B. Parsons, 1999: A proposed mechanism for the intrusion of dry air into the tropical western Pacific region. *J. Atmos. Sci.,* **56,** 1524–1546.

Zhang, C., 2005: Madden–Julian oscillation. *Rev. Geophys.,* **43,** RG2003, doi:10.1029/2004RG000158.

Zhu, H., H. Hendon, and C. Jakob, 2009: Convection in a parameterized and super-parameterized model and its role in the representation of the MJO. *J. Atmos. Sci.,* **66,** 2796–2811.